Controllable adhesive mechanisms via the internal fibers in soft footpads of honeybees

Lulu Liang [a], Jieliang Zhao [a,*], Qun Niu [a], Li Yu [a], Zhiyun Ma [a], Xiangbing Wu [a], Wenzhong Wang [a,**], Shaoze Yan [b]

[a] School of Mechanical Engineering, Beijing Institute of Technology, Beijing, 100081, PR China
[b] Division of Intelligent and Biomechanical Systems, State Key Laboratory of Tribology, Department of Mechanical Engineering, Tsinghua University, Beijing, 100084, PR China

ARTICLE INFO

ABSTRACT

The dynamic adhesive systems in nature have served as inspirations for the development of intelligent adhesive surfaces. However, the mechanisms underlying the rapid controllable contact adhesion observed in biological systems have never been adequately explained. Here, the control principle for the unfolding adhesive footpads (alterable contact area) of honeybees is investigated. The footpads can passively unfold, even without neuro-muscular reflexes, in response to specific dragging activity (generating shear force) toward their bodies. This passive unfolding is attributed to the structural features of the soft footpads, which cooperate closely with shear force. Then, the hierarchical structures supported by numerous branching fibers were observed and analyzed. Experimental and theoretical findings demonstrated that shear force can decrease fibril angles with respect to the shear direction, which consequently induces the rotation of the interim contact area of the footpads and achieves their passive unfolding. Furthermore, the decrease in fibril angles can lead to an increase in the liquid pressure within the footpads, and subsequently enhance their unfolding. This study presents a novel approach for passively controlling the contact areas in adhesive systems, which can be applied to develop various bioinspired switchable adhesive surfaces.

1. Introduction

Over the past decade, natural adhesive systems have garnered significant attention due to their strong and reversible adhesion on nearly all known surfaces. Examples include the hierarchical setae of the geckos, which generate van der Waals force to support its weight [1], the hexagonal patterns of the tree frogs, which form capillary force on humid surfaces [2], and the suckers of the octopus and leeches, which adsorb on the dry and wet substrates with negative pressure [3,4]. Inspired by these adhesive systems, various artificial adhesive surfaces have been employed in smart devices, such as intelligent grippers [5], wearable electronic skins [6], and wound dressings [7,8]. Despite their rapid development, artificial adhesive surfaces suffer from long switching times between attachment and detachment, which range from seconds to minutes [9–11]. Whereas, the adhesive systems of many insects, such as ants and honeybees, exhibit rapid switching due to their highly rapid stride frequencies [12,13]. These dynamic biological adhesive systems

can be attributed to precise control of adhesive strength and contact area. Some insects, such as ants [14], can sometimes rapidly change and control their contact areas in less than a millisecond. Therefore, gaining further insight into the mechanisms that regulate contact areas in insect adhesive systems is highly beneficial to improve the rapid control of artificial adhesives.

The alterable contact area of footpads can be passively adjusted by shear force during attachment and detachment when pressed on the ground. For example, the hairy adhesive pads of certain organisms such as geckos [8], spiders [15], and flies [16] possess numerous spatulated setae [13], which can be translated into full contact with a substrate by a shear force toward their bodies [13,17]. Other smooth adhesive pads evolve different strategies in response to shear force. Stick insects possess a fibrous inner structure in the procuticle of their footpads [18] that produces a lateral expansion of the contact area with hydraulic function in the pads [18,19], while the drag activity (generating shear force) reduces the fibrous angle between the fibers and the substrate. Similarly,

the dense array of nanopillars in the toe pads of tree frogs improves adhesion and friction [20,21], which is likely proportionate to the increment of the contact area resulting from the changing angles between the pillars and the pad's surface by shear force [20,22]. Specifically, some insects possess a smooth footpad that can switch between folded and unfolded morphologies [13]. The adhesive pads of ants and bees have been observed to rapidly unfold in response to imposed shear force, and a hypothetical pulling model has been established to describe this function [23]. This passive unfolding retraction in ants can sometimes occur within less than a millisecond [14], which is much shorter than the neuronally controlled reflexes in insects [24]. Although these regulatory mechanisms of contact area via shear forces have been widely observed in different adhesive systems, especially the folding adhesive pads, corresponding physical models have not yet been fully developed and verified.

Arolium is an adhesive footpad of honeybees characterized by its rapid unfolding and folding capacity. In this study, the rapid evolution processes of the inner structures in the honeybee arolium were investigated and the inherent relationships between the contact area and shear force were explored. Firstly, the structures and deformations of the honeybee arolium were observed during attachment and detachment, and the collaboration of the contact area and lateral expansion of unfolded arolium controlled by shear force was investigated. Secondly, the morphologies of the outer and inner structures of arolium were characterized, and the unfolding and the folding mechanisms of arolium were theoretically analyzed. Finally, Finite Element Method (FEM) models were established to verify the theoretical and experimental analyses.

2. Materials and methods

2.1. Study insects

Female adult honeybees (*Apis mellifera* L.) were collected from Beijing's Fragrant Hills Park and transported to the laboratory of the Beijing Institute of Technology, Beijing, China. All animal experiments complied with the ARRIVE guidelines and were carried out in accordance with the U.K. Animals (Scientific Procedures) Act, 1986 and associated guidelines, EU Directive 2010/63/EU for animal experiments. No endangered or protected species were used in this investigation.

2.2. Adhesion measurements and contact area observations of honeybee arolium

An experimental setup for measuring the adhesion and contact area of honeybee arolium observation was performed with a bespoke test system. The system consists of a microscope equipped with a high-speed camera (Memrecam HX-7S, NAC, Japan) for contact area observations with a sampling frame rate of 1000 fps. Besides, two load cells (GSO-10 and GSO-50, Transducer Techniques, USA) were incorporated to measure the normal and shear adhesion with a sampling frequency of 1 kHz. The experimental honeybee was restricted on a beam and then brought into contact with the fixed glass slide on the load cells at a slow speed.

2.3. Visualization of resilin in the honeybee arolium

Honeybees were freshly frozen at $-70°C$, and then the legs with arolium were immersed in glycerine after thawing. The glycerine-coated arolium was transferred to a glass slide and covered externally with glycerine and a high-precision coverslip. Subsequently, the sample was examined with the confocal laser scanning microscopy system (N-SIM E, Nikon, Japan) equipped with four lasers (laser lines; 405 nm, blue; 488 nm, green; 561 nm, yellow and red; 640 nm, red). Finally, the resilin autofluorescence of honeybee arolium was observed using the 405 nm laser line, and then bright-field images and wide-field fluorescence images were captured and superimposed [25].

2.4. Observation of inner structures in honeybee arolium

The inner structures in the arolium were obtained using focused ion beam (FIB) treatment, which consisted of the following steps.

Sample preparation: Adult honeybees were narcotized at $4°C$, and then the legs of honeybees were dissected and immersed in pentanediol stationary solution (2.5%) for 4 h at $5°C$. Then, the samples were rinsed with phosphate buffer solution (PBS: 0.1 M, pH7.3 ± 0.1) three times for 3 min each and dehydrated through a series of gradient ethanol (40%, 50%, 70%, 80%, 90%, 95%, and 100%) for 10 min each. Subsequently, the samples were dried with a critical point dryer (EM CPD300, Leica, Wetzlar, Germany).

Sample treatment and observation: The samples were affixed on the workbench using conductive adhesive tape and sputter-coated with a 50 nm layer of gold-palladium. The samples were then transferred to the FIB-SEM system (Helios G4 UC, FEI, USA). For each arolium, a series of rectangular windows (10 μm × 10 μm) were cut at 10 nA and the cutting edges were trimmed at 0.1 nA [26]. Besides, the sectional SEM images of honeybee arolium were captured at 5 kV and 0.1 nA.

### 2.5. Unfolding honeybee arolium by increased pressure

The hind legs of the honeybees were amputated, and then the arolium with the distal tarsal segment (served as a sample for observation) was carefully removed. The sample was transferred onto the microscope stage and affixed on a glass slide with double-sided tapes. Then, the certain deionized water was inserted into the tarsal segment of the sample using a micromanipulator (3-000-024-R, Drummond, USA) equipped with an injection needle, and the connector was sealed by applying a droplet of fast-hardening glue. In addition, the injection needle was connected to a programmable nanoliter injector (Nanoject III, Drummond, USA), which controls the injection speed at 5 nL/s. Keeping this process and observing the unfolding of the honeybee arolium.

3. Results and discussion

3.1. Evolution process of contact area passively controlled by dragging movement

Honeybees exhibit preeminent capacities to easily traverse smooth artificial surfaces or flower petals for drinking and foraging owing to their highly dynamic wet adhesion. These superior capacities including rapid attachment and detachment occur millions of times during their lifetime. Fig. 1A illustrates the experimental setup for observing the arolium morphologies and measuring the adhesive forces of honeybees during adhesive periods. As shown in Fig. 1B, the foldable honeybee arolium constantly changed its contact area (folding and unfolding) during its attachment and detachment process (Video S1). Due to this rapid evolution process, the adhesive force of honeybees (including normal and shear adhesion) exhibited highly dynamic performances (Fig. 1C), reflecting an adhesive period less than 1 s though the movement of the experimental honeybees was restricted (Fig. 1A). This is because the adhesive forces can be attributed to the product of adhesive strength and changing contact area. Besides, the negative value of normal adhesion indicated the preload during attachment (Fig. 1C), which is corresponding with the pre-contact observed in the changing contact area (Fig. 1C and D).

The folding and unfolding of the honeybee arolium were controlled by the dragging movement of the tarsus (Fig. 1B and D), generating shear force parallel to the dragging direction. After the pre-contact, when the dragging movement toward the proximal direction happened, the foldable arolium simultaneously unfolded over a period of approximately 350 ms. In contrast, when the aforementioned dragging operation ceased or a contrary movement started, the arolium folded rapidly within about 300 ms. Besides, the pre-contact and newly formed contact areas were fixed on the substrate owing to their adhesion. To further ascertain the
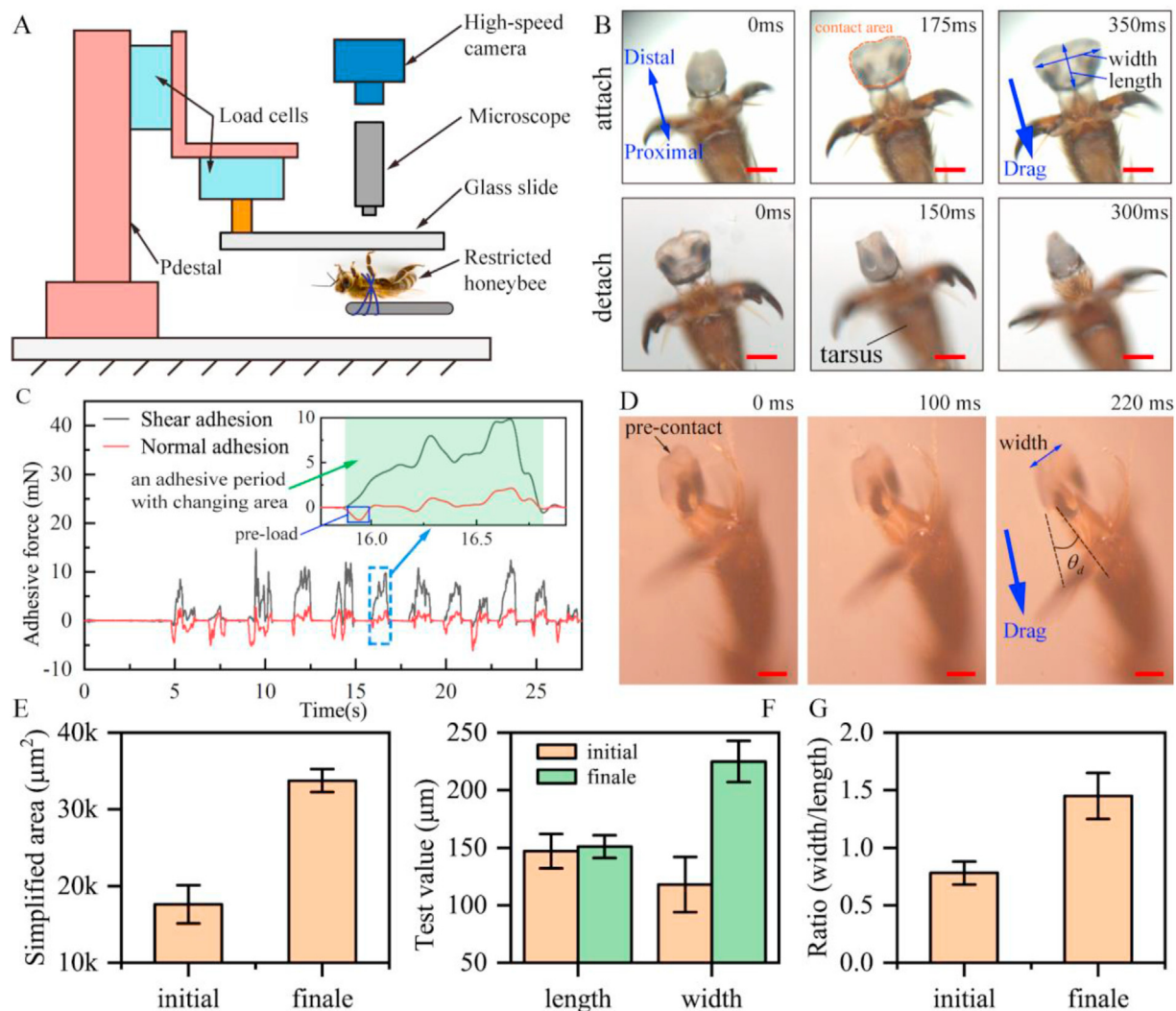
Fig. 1. The rapid folding and unfolding of arolium passively controlled by shear force. (A) Schematic of the configuration used to measure the arolium's adhesion and observe the contact area with restricted movement. Rapid changes of the morphologies (Bottom) (B) and adhesion of a living honeybee arolium (C) during attachment and detachment. The scale bar is 100 μm. (D) Unfolding arolium of an anatomical leg switched by the artificial dragging movement (Lateral). The scale bar is 100 μm. Simplified contact area (E) (length × width), structural size (F) (length and width), and aspect ratio (G) (width/length) of the honeybee arolium after the shear dragging movement.

effects of shear force on the unfolding arolium rather than the neural operation, a freshly amputated leg with honeybee arolium was observed at the lateral view when the dragging movement operated. Similarly, the arolium unfolded passively (without any muscular action) in response to the shear force controlled by the artificial dragging movement (Fig. 1D) (Video S2).

Furthermore, the changes in the contact area of the honeybees are closely related to the lateral extension of their arolium (Fig. 1E–G). The increase in contact area (Fig. 1E) mainly resulted from the significant increase in the lateral width of the arolium during unfolding, whereas the longitudinal length remained generally constant (Fig. 1F). Meanwhile, the aspect ratio (width/length) rose from 0.78 to 1.45 (Fig. 1G). These results indicate that the increases in the contact area of honeybees were primarily induced by the lateral expansion of the arolium, which was passively (i.e. without any muscular action) controlled by the shear force toward the proximal direction.

3.2. Morphological observation of honeybee arolium

The mechanism underlying the passive unfolding of the honeybee arolium was investigated by first focusing on its morphology and mate-rial properties (Fig. 2). The honeybee's adhesive system mainly consisted of the arolium, arcus, and manubrium (Fig. 2A). The distributed elastic arcus (Fig. 2A) acts as the primary internal supports for the soft arolium and contributes to the rapid detachment via the release of elastic energy stored from its deformation (accompanied with the unfolding arolium) caused by the shear force. Besides, the bilateral edges of the fully unfolding arolium remain folded (with an included angle close to 180° in Fig. 2B) rather than entirely spreading out on the substrate. Then, the thin-film peeling theory was used to explain the functions of the folding edge of the arolium (Fig. 2B and C). Based on the model of Kendall [27], the peeling force (F_p) can be estimated as

$$F_p = \frac{E_t b}{1 - \cos\theta},\tag{1}$$

where θ is the peeling angle (included angle), b is the width of the elastic membrane, and E_t is the experimental adhesive energy required to fracture per unit area which can be formulated in terms of the work of adhesion (W) [28,29]. Therefore, the larger peeling angle needs a smaller peeling force, resulting in a lower requirement of the strain energy (arcus and arolium) stored from the shear force, and then promotes the folding of arolium during detachment. Moreover, the arolium has
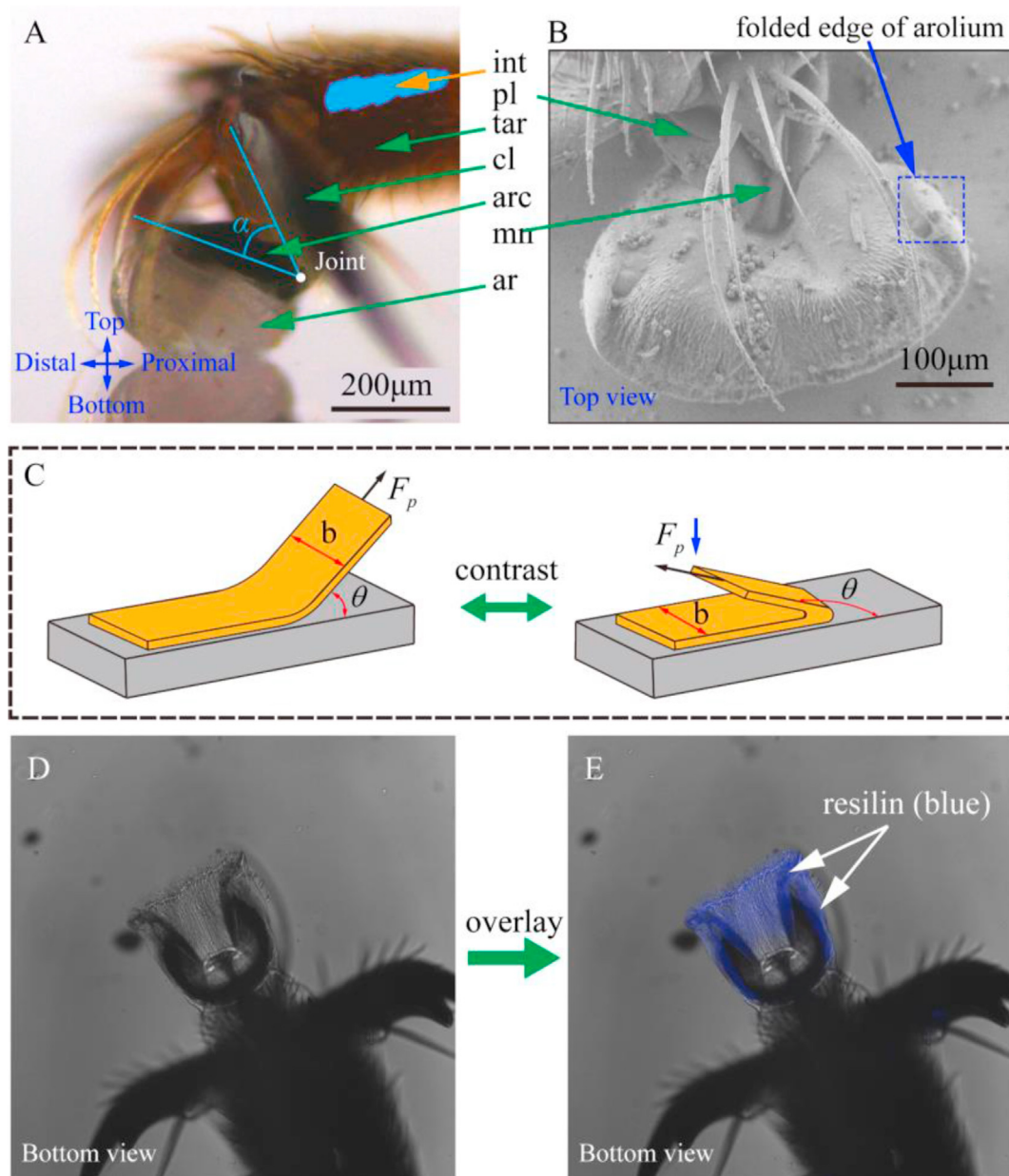
Fig. 2. Microscopy images of structural morphologies of honeybee arolium. Lateral view of folded arolium (A) via stereoscope and rotating top view of unfolded arolium (B) via Cryogenic scanning electron microscopy (Cryo-SEM). (C) Schematic of the peeling theory, indicating the functions of the folded edge of the arolium. Overlay of a bright-field micrograph (Bottom) (D) and a wide-field fluorescence micrograph (Bottom) (E) showing the resilin autofluorescence in arolium. int: inner tendon, pl: planta, tar: tarsus, cl: claw, arc: arcus, mn: manubrium, ar: arolium.

been proven to process rotatable architecture around a certain joint (Fig. 2A), which is controlled by the synergistic effects of the arcus and the inner shrinkable tendon (blue schematic in Fig. 2A) [30,31]. However, the neuro-muscular activity still cannot explain the passive lateral extension of the arolium. Material properties are another important feature that influences the folded states of the honeybee arolium. As shown in Fig. 2D and E, resilin autofluorescence (blue region) is evenly distributed throughout the arolium. Resilin, a protein with high resilience that has been already found in arthropod joints and deforming cuticles [32,33], exhibits remarkable resistance to mechanical fatigue under repetitive loading conditions. Additionally, the arcus presents an arched black region while other regions of the arolium are nearly transparent (Fig. 2A and B). This factor suggests that the elastic modulus of the arcus is much higher than other regions of the arolium, which is a reasonable conclusion based on its supportive role in the arolium.

Although the aforesaid construct the basics (such as the high resilience of arolium) of the folding and unfolding arolium during attachment and detachment, they are still insufficient to fully elucidate the unfolding process of arolium passively controlled by shear force.

3.3. Different morphologies of branching fibers within arolium responding to shear force

The fibrous structures within the arolium have been shown to play a crucial role in controlling the contact area of insects in response to shear forces, such as the arolium of stick insects which lacks folding capacities [18]. Therefore, to comprehend the folding and unfolding mechanism of the honeybee arolium, its inner 3D structures were investigated (Fig. 3). Various focused ion beam (FIB) partial cuttings of the honeybee arolium were observed to verify the accurate orientation of fibers. These fibers,
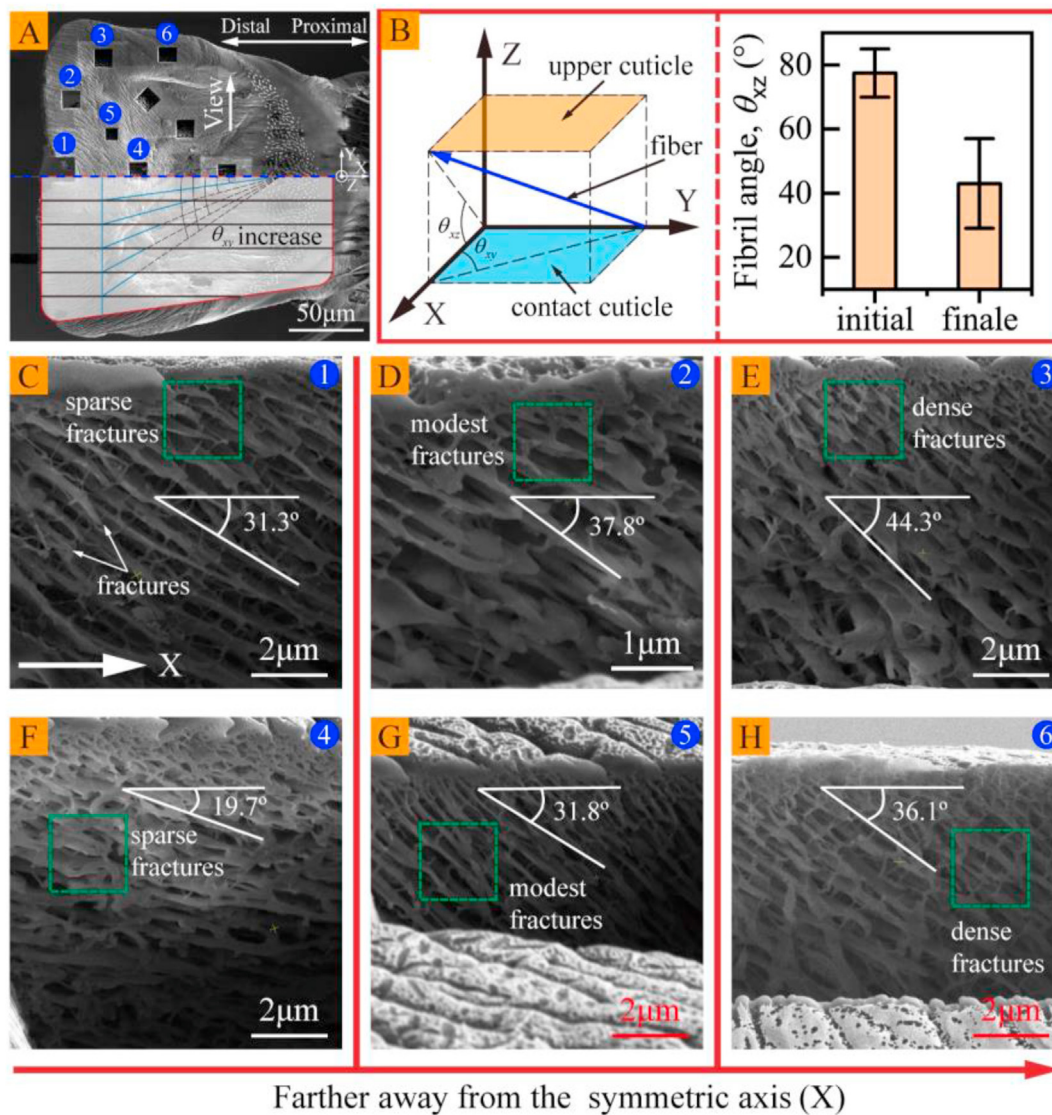
Fig. 3. Scanning electron microscopy images of the branching fibrous structure within the unfolded arolium of a honeybee via focused ion beam (FIB). (A) Bottom view of unfolded arolium with the schematic direction of different fibers. (B) 3D schematic of a single fiber showing the spatial angle compared to the drag direction. (C–H) Fibers slanted toward the contact cuticle with the observing view rotated 40° around the axis (X). (C-E) and (D-F) in response to the location further away from the symmetric axis.

which filled the outer cuticle layer of the arolium and were connected via the smaller branched fibers (Fig. 3C–E), were spatially orientated toward the shear direction (X-axis) (Fig. 3A and B). For the first feature of the fibers projecting on the X-Z plane, the vertical fibril angles (θ_{xz}) between the fibers and epicuticle were approximately 29°–57° (Fig. 3B), which were obtained through a geometric transform of the observed angles (Fig. 3C–H) considering a sloping angle of 40° during FIB observation. Besides, these angles increased for fibers located further away from the symmetric axis of the arolium, ranging from 31.3° to 44.3° in Fig. 3C–E and 19.7°–36.1° in Fig. 3F–H. As arolium unfolded, θ_{xz} descreased compared to the nearly upright fibers ($\theta_{xz} \approx 70-85°$) of the folded arolium [26,34].

Another feature of the fibers in the honeybee arolium has not been observed in other insects before. Projecting on the X–Y plane, the horizontal fibril angles (θ_{xy}) between fibers and the shear direction (X-axis) are illustrated in Fig. 3B. Angle θ_{xy} increased gradually for fibers located further away from the symmetric axis of the arolium (Fig. 3B), which was indirectly supported by the existence and increasing density of fibrous

fractures (Fig. 3C–E and Fig. 3F–H). For example, the number of fibrous fractures in Fig. 3E is greater than that in Fig. 3C (about 10 > 4, green region in Fig. 3C and E), which means the increasing density of fibrous fractures, and then verifying that larger fibril angles θ_{xy} is corresponding to the location further away from the symmetric axis.

3.4. Evolution process of fibers and contact area controlled by shear force

The effects of shear force in controlling the contact area of honeybees were analyzed by using theoretical models to reveal the evolution process of the inner hierarchical structures of the arolium (Fig. 4). Fig. 4A shows the various forces acting on the arolium including the capillary and friction force. Concretely, the capillary force (F_{cap}) can be expressed as the summation of the Young-Laplace pressure effect and surface tension [35] as represented by Equation (2),

$$F_{cap} = \Delta P\pi R^2 + 2\pi\gamma R \sin\theta, \qquad (2)$$
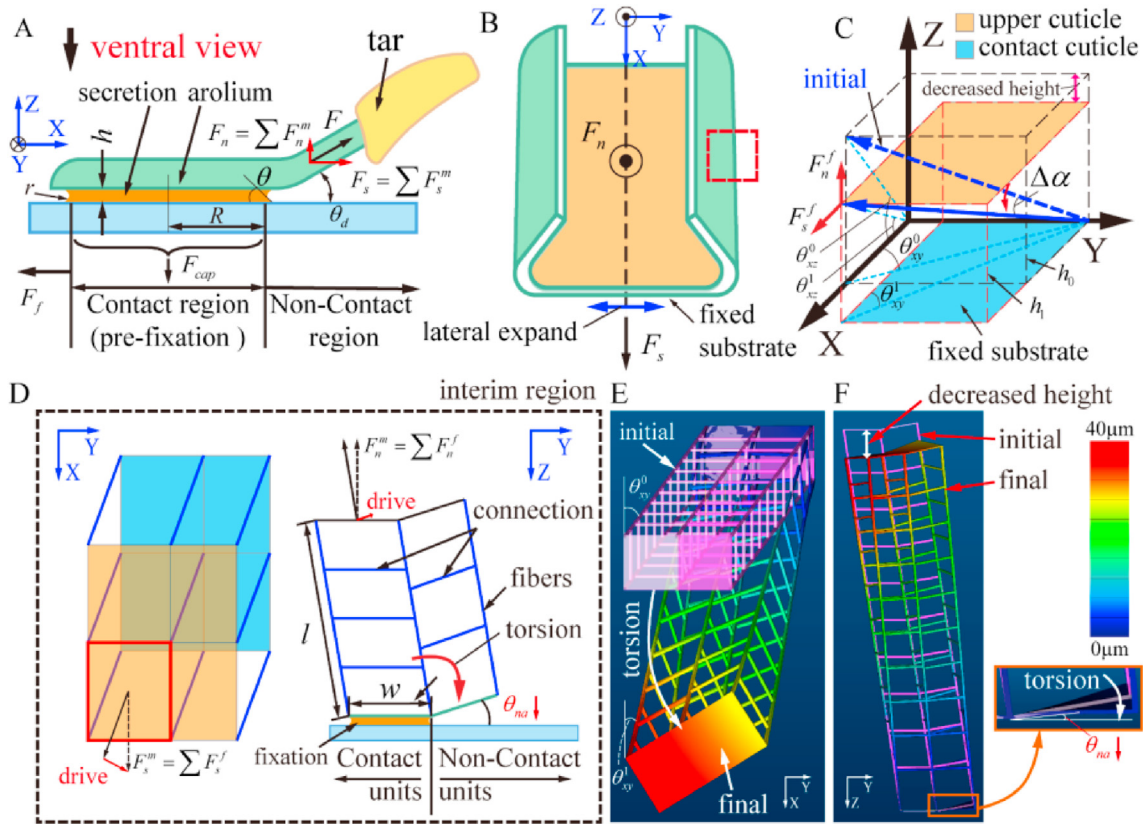
Fig. 4. The theoretical models for the passive increase of contact area in honeybee hierarchical arolium. (A) The various forces in the arolium during attachment and detachment. (B–D) Different performances of the partial contact area with deformable fibers (C) as a response to shear force. (E–F) FEA simulations of fibers and hierarchical structures to verify the evolution process of fibers and contact area controlled by shear force.

where γ is the surface tension of the liquid secretion, θ is the contact angle between the contact substrate and the liquid secretion, and ΔP is the Young-Laplace pressure which can be estimated as [35]

$$\Delta P = \gamma \left(\frac{1}{R} + \frac{1}{r} \right), \tag{3}$$

where R and r are the two meniscus radiuses of the liquid bridge. Then, based on the thinner liquid film, the friction (F_f) (with a friction coefficient, μ) can be estimated as [36]

$$F_f = \mu F_{cap} \tag{4}$$

These two forces contribute to resisting shear force during attachment and detachment and peculiarly exhibit the pre-fixation as the basics of the passive unfolding during arolium.

Considering the elastic and hierarchical structures of arolium (Figs. 2E and 3C), the shear force cannot be directly transmitted to the contact interface, which subsequently affects the arolium's unfolding. Then, micro-units in the interim region between the contact and non-contact regions (Fig. 4B-D) were selected to future analyze the evolution process of fibers controlled by shear force, which are more prone to bending rather than stretching due to their greater slenderness ratio (length/diameter >20) (Fig. 3C). Firstly, the rapid response of a single fiber to the internal shear force was analyzed (Fig. 4C). Due to the smaller dragging angle (θ_d) (Figs. 1D and 4A) during arolium unfolding, the shear component force on a fiber $[F_s^f(\theta_{xy}, \theta_{xz})]$ is much greater than the normal component force $[F_n^f(\theta_{xy}, \theta_{xz})]$ transformed from the dragging action, which leads to the decrease of fibril angles (θ_{xy} and θ_{xz} in Fig. 4C) with a fixed boundary resulting from the capillary and friction force. These

rapid changes in fibers are coincident with a previous study about arolium in insects [18].

Consequently, the evolution processes of a single fiber were extended to the interim region of arolium (Fig. 4B and D). Due to the flexible fibers (Fig. 4C), the micro-units (including fibers, upper and contact cuticles) exhibit the consequential torsional deformation driven by shear force (Fig. 4D). For a square micro-unit, the resultant forces (F_s^m, F_n^m) (supported by four fibers) can be expressed as

$$F_s^m = \sum F_s^f(\theta_{xy}, \theta_{xz}), \tag{5}$$

$$F_n^m = \sum F_n^f(\theta_{xy}, \theta_{xz}). \tag{6}$$

The fixed foundation of the contact cuticle and fibers, resulting from capillary force and friction, can induce the torsion of the left unit (contact region) towards the lower right corner when cooperating with the component forces of F_s^m and F_n^m (red schematic forces in Fig. 4D) perpendicular to the fibers. Considering the interconnections of fibers by smaller branched fibers, the right unit (non-contact region) will be subsequently propelled in the right direction (Fig. 4D).

Then the torsion of the right unit induces a decrease in the non-contact angle (θ_{na}), resulting in the generation of a new contact region when θ_{na} approaches zero or the generation of a new capillary force. Thus, the arolium's unfolding process is ultimately achieved and induced by shear force. To prove the theoretical torsions, a Finite Element Method (FEM) model was developed, using simulation software (Creo 5.0, PTC, USA), with the boundary conditions and applied forces as depicted in Fig. 4D. Under these forces, the micro-units exhibit the torsions on the X–Y and Y-Z planes (Fig. 4E and F), particularly the torsion of the right unit (non-contact region) towards the lower right direction, which aligns

with the mechanical prediction (Fig. 4D). Besides, the decrease in total height responding to the shear force (Fig. 4F) indirectly demonstrates the reduction in the fibril angle (θ_{xz}) (Fig. 4C). Along with the decrease in fibril angle (θ_{xy}) (Fig. 4F), the observed decreases in the fibril angles (Fig. 3) induced by shear force were verified. Moreover, the decrease in the non-contact angle (θ_{na}) is observed (Fig. 4F), indicating the unfolding of the arolium. Notably, this passively controllable mechanism of the contact area is an ingenious energy-saving system that enables honeybees to transform gravity into shear force when attaching to vertical surfaces.

3.5. Effects of the inner pressure on the unfoldment of honeybee arolium

The decreases in the fibril angles possess the potential to influence the pressure of the liquid surrounding the inner fibers, thereby enhancing the unfolding process of the honeybee arolium. Fig. 5A illustrates the experimental setup to investigate the effects of the alterable inner pressure of arolium. Primarily, the soft arolia of insects are liquid-filled materials without any inner air [37], and the inner liquid is incompressible under normal pressure and temperature. To indirectly increase the inner pressure of arolium, a tiny volume of deionized water was gradually injected into the tarsal segments of honeybees (Fig. 5A and B). Meanwhile, the freshly removed arolium unfolded in response to this injecting process (Fig. 5B). The two observed unfolded states indicate the enhancement of the increasing inner pressure on the unfolding of the honeybee arolium (Fig. 5B). This result is consistent with a previous study that demonstrated the arolium inflation through increased pressure in ants (*O. smaragdina*) [23].

To investigate the effect of the alterable fibril angles on the inner pressure, a simplified partial model of the honeybee arolium was established, comprising bionic fibers and inner liquid (Figs. 3 and 4C). The decreases in the fibril angles (θ_{xy} and θ_{xz}) controlled by the shear force

resulted in a decrease in the model's height (Fig. 4F), which subsequently leads to a change in the liquid form considering the constant volume of liquid (Fig. 5C). Here, the Bernoulli equation [38] was employed to estimate the pressure difference between the two states (Fig. 5D) as

$$P_0 + \frac{1}{2}\rho V_0^2 + \rho g h_0 = P_1 + \frac{1}{2}\rho V_1^2 + \rho g h_1 = C \tag{7}$$

where P is the inner pressure, ρ is the liquid density, V is the local velocity, g is the gravity acceleration, h is the vertical height, C is a constant, and subscripts 0 and 1 represent the different states. Considering the steady states of the initial and final state, the local velocity (V) can be set to zero. Then the decrease in height (h) can lead to an increase of the inner pressure ($\Delta P_{in} = \rho g(h_0 - h_1)$), which likely promote the unfolding of the arolium.

However, generalizing this function to the unfolding of the honeybee arolium necessitates assuming a constant volume of the inner liquid within the arolium. In fact, this assumption is supported by the slow volume change of the liquid as it permeates through the epidermal cells on the honeybee arolium [17]. Subsequently, to model the liquid-structure interactions, including the liquid's pressure and the deformation induced by shear force, the coupled Euler-Lagrange (CEL) approach was adopted (Fig. 6A) [39]. The liquid model, discretized utilizing the EC3D8R element in the Eulerian domain, was carried out using the Explicit method in the simulation software (Abaqus 2021, Dassault Systemes, France) with defined boundary conditions and applied loads (Fig. 6A). Fig. 6A illustrates the evolution process of the liquid pressure and the mechanical deformations induced by shear force. During the loading process, the peak liquid pressure rapidly rises and falls, eventually achieving a steady pressure greater than the initial pressure (Fig. 6B). This rapid rise in peak pressure is driven by the sudden mechanical deformations induced by shear force, and is subsequently
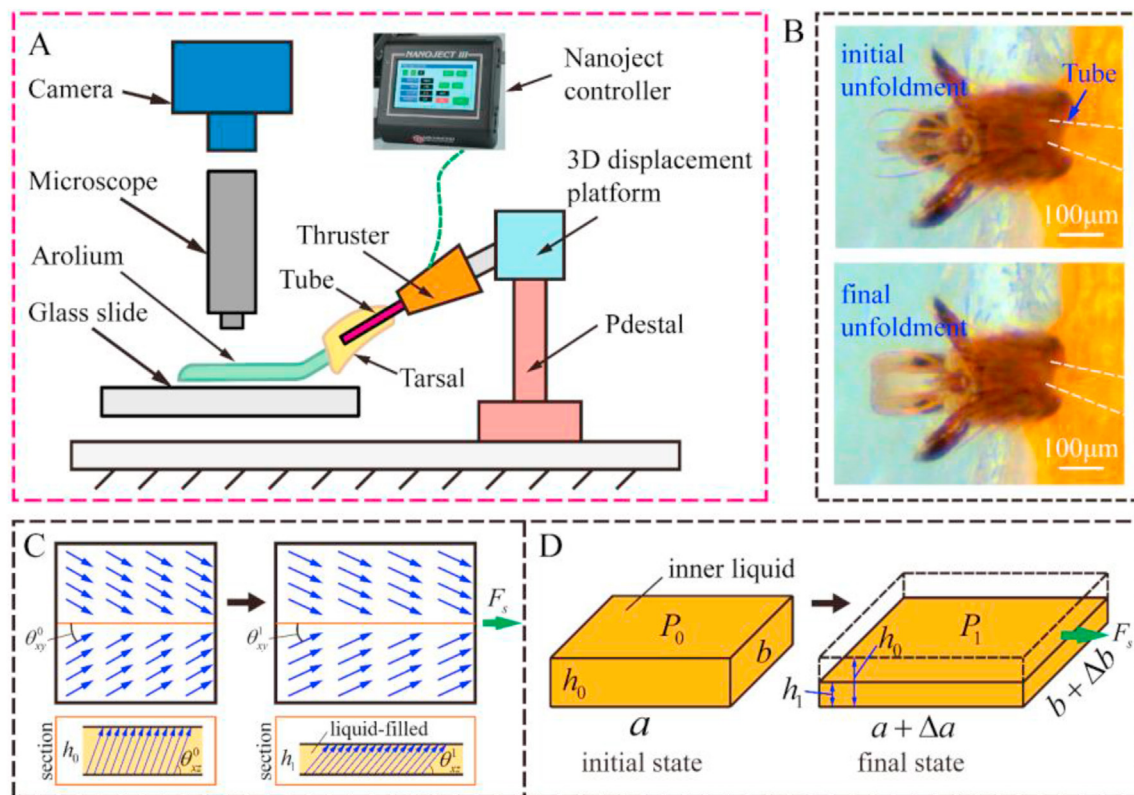
Fig. 5. Schematic of the effects of the inner pressure on the unfolding of the honeybee arolium. (A) The experimental setup to investigate the connection between the inner pressure and the arolium's unfolding. (B) Experimental results showed the lateral unfolding of the arolium caused by the increase in the inner pressure. (C) The changes in the liquid form within the arolium respond to the changing fibril angles and shear force. (D) A simplified model shows the increase in the inner pressure resulting from the change in the liquid form.
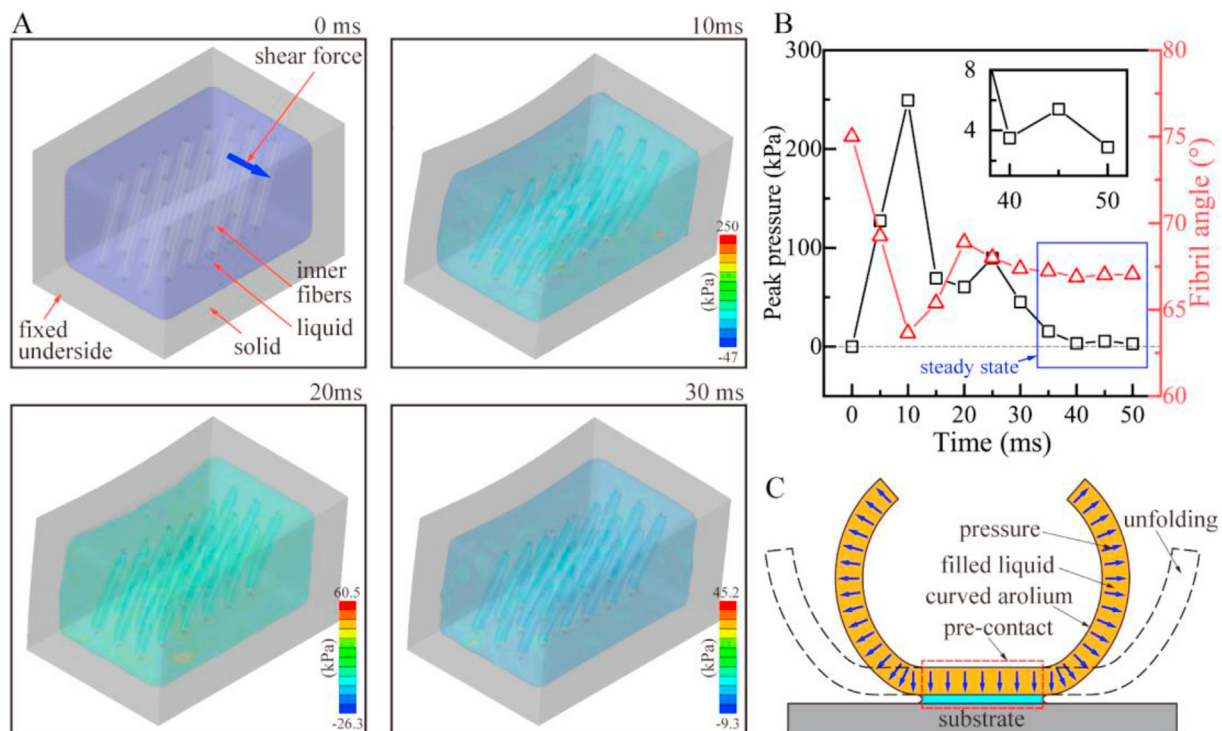
Fig. 6. FEA simulations for the increasing inner pressure caused by shear force. (A) The evolution process of the liquid pressure and the mechanical deformations. (B) The changes in the liquid pressure and inner fibril angle. (C) Unfolding arolium caused by the increase of inner pressure.

neutralized by other liquids. However, the stable increased pressure (steady state), corresponding to the decrease in height and fibril angle caused by shear force (Fig. 6B), aligns with the predication of Eq. (7) (Fig. 5D). In conclusion, the increase in liquid pressure is proved to be induced by shear force. Considering the cantilever beam-like structures of the honeybee arolium, characterized by bilateral bends and intermediate fixation (Figs. 2A and 6C), the increased pressure induced by shea force can further enhance the increase in the lateral width (lateral unfolding) rather than the proximal–distal length. This observation is unified with the observed unfolding of the honeybee arolium under the experimentally applied pressure (Fig. 5B).

4. Conclusion

The exceptional dynamic adhesion of many insects is closely related to the variable morphologies of their unfolded arolium, which are rapidly controlled by their shear actions. In this study, the passive controllable mechanisms of the unfolding honeybee arolium (i.e. contact area) were investigated, allowing honeybees to respond to sudden environmental disturbances. Experimental results (Fig. 1) showed that the unfolding arolium (lateral extension) and the increasing contact area, are passively controlled by shear force. Then the mechanical properties of the arolium, especially including its inner branching fibers, were investigated (Fig. 3). Theoretical model and experiments demonstrated that shear force can lead to a decrease in fibril angles, and then result in the torsion of the arolium's cuticles, which forming a new contact region and achieve the unfolding of the arolium.

Additionally, the alterable pressure within the liquid-filled arolium was found to enhance its unfolding. The experimental preload to the inner pressure verified its effects on the unfolding of the honeybee arolium. Besides, the increasing pressure resulting from the decreasing height (decreasing fibril angles) controlled by the shear force, was theoretically revealed using the Bernoulli equation and simulated through Finite Element Method (FEM) (Figs. 5 and 6). The unfolding of arolium caused by the increased inner pressure is coincident with the

observed lateral extension (Fig. 1). Notably, this passive controllable mechanism of the contact area in the honeybee arolium offers new perspectives for high dynamic adhesion, and can be applied to bionic switchable applications, such as intelligent transports and climbing robots.

Credit author statement

Lulu Liang: conceptualization, performing experiments, analysis of data, writing the original draft, reviewing and editing the manuscript. **Jieliang Zhao**: conceptualization, analysis of data, reviewing and editing the manuscript. **Qun Niu**: performing the experiment of adhesion measurement, analysis of data. **Li Yu**: performing the experiment of observing inner fibers, analysis of data. **Zhiyun Ma**: performing FEM simulation. **Xiangbing Wu**: performing FEM simulation. **Wenzhong Wang**: reviewing and editing the manuscript. **Shaoze Yan**: reviewing and editing the manuscript.

Declaration of competing interest

The authors declare that they have no known competing financial interests or personal relationships that could have appeared to influence the work reported in this paper.

Data availability

No data was used for the research described in the article.

Acknowledgements

the Opening Project of State Key Laboratory of Tribology, Tsinghua University (NO. SKLTKF20B06).

Appendix A. Supplementary data

Supplementary data to this article can be found online at https://doi.org/10.1016/j.mtbio.2023.100704.

References

[1] A.Y. Stark, D.M. Dryden, J. Olderman, K.A. Peterson, P.H. Niewiarowski, R.H. French, A. Dhinojwala, Adhesive interactions of geckos with wet and dry fluoropolymer substrates, J. R. Soc. Interface 12 (108) (2015), 20150464, https://doi.org/10.1098/rsif.2015.0464.

[2] W. Federle, W.J.P. Barnes, W. Baumgartner, P. Drechsler, J.M. Smith, Wet but not slippery: boundary friction in tree frog adhesive toe pads, J. R. Soc. Interface 3 (10) (2006) 689–697, https://doi.org/10.1098/rsif.2006.0135.

[3] S. Baik, D.W. Kim, Y. Park, T. Lee, S. Ho Bhang, C. Pang, A wet-tolerant adhesive patch inspired by protuberances in suction cups of octopi, Nature 546 (7658) (2017) 396–400, https://doi.org/10.1038/nature22382.

[4] S. Li, Y. Zhang, X. Dou, P. Zuo, J. Liu, Hard to be killed: load-bearing capacity of the leech Hirudo nipponia, J. Mech. Behav. Biomed. Mater. 86 (2018) 345–351, https://doi.org/10.1016/j.jmbbm.2018.07.001.

[5] Y. Chen, J. Meng, Z. Gu, X. Wan, L. Jiang, S. Wang, Bioinspired multiscale wet adhesive surfaces: structures and controlled adhesion, Adv. Funct. Mater. 30 (5) (2019), 1905287, https://doi.org/10.1002/adfm.201905287.

[6] D. Drotlef, M. Amjadi, M. Yunusa, M. Sitti, Bioinspired composite microfibers for skin adhesion and signal amplification of wearable sensors, Adv. Mater. 29 (28) (2017), 1701353, https://doi.org/10.1002/adma.201701353.

[7] S. Baik, H.J. Lee, D.W. Kim, J.W. Kim, Y. Lee, C. Pang, Bioinspired adhesive architectures: from skin patch to integrated bioelectronics, Adv. Mater. 31 (34) (2019), 1803309, https://doi.org/10.1002/adma.201803309.

[8] S. Jiao, X. Zhang, H. Cai, S. Wu, X. Ou, G. Han, J. Zhao, Y. Li, W. Guo, T. Liu, W. Qu, Recent advances in biomimetic hemostatic materials, Mater. Today Bio 19 (2023), 100592, https://doi.org/10.1016/j.mtbio.2023.100592.

[9] D. Tan, X. Wang, Q. Liu, K. Shi, B. Yang, S. Liu, Z.S. Wu, L. Xue, Switchable adhesion of micropillar adhesive on rough surfaces, Small 15 (50) (2019), 1904248, https://doi.org/10.1002/smll.201904248.

[10] S. Xia, Y. Chen, J. Tian, J. Shi, C. Geng, H. Zou, M. Liang, Z. Li, Superior low-temperature reversible adhesion based on bio-inspired microfibrillar adhesives fabricated by phenyl containing polydimethylsiloxane elastomers, Adv. Funct. Mater. 31 (26) (2021), 2101143, https://doi.org/10.1002/adfm.202101143.

[11] H. Yi, S.H. Lee, M. Seong, M.K. Kwak, H.E. Jeong, Bioinspired reversible hydrogel adhesives for wet and underwater surfaces, J. Math. Chem. B 6 (48) (2018) 8064–8070, https://doi.org/10.1039/c8tb02598c.

[12] J. Zhao, F. Zhu, S. Yan, Honeybees prefer to steer on a smooth wall with tetrapod gaits, J. Insect Sci. 18 (2) (2018), https://doi.org/10.1093/jisesa/iey038.

[13] W. Federle, D. Labonte, Dynamic biological adhesion: mechanisms for controlling attachment during locomotion, Phil. Trans. R. Soc. B 374 (2019), 20190199, https://doi.org/10.1098/rstb.2019.0199.

[14] T. Endlein, W. Federle, Ants can't be knocked off: a 'preflex' as an extremely rapid attachment reaction, Comp. Biochem. Physiol. A 153 (2009) S138 (Abstract).

[15] J.O. Wolff, S.N. Gorb, Radial arrangement of Janus-like setae permits friction control in spiders, Sci. Rep. 3 (1) (2013), https://doi.org/10.1038/srep01101.

[16] S. Niederegger, S. Gorb, Tarsal movements in flies during leg attachment and detachment on a smooth substrate, J. Insect Physiol. 49 (6) (2003) 611–620, https://doi.org/10.1016/S0022-1910(03)00048-9.

[17] W. Wang, Y. Liu, Z. Xie, Gecko-like dry adhesive surfaces and their applications: a review, J. Bionic Eng. 18 (5) (2021) 1011–1044, https://doi.org/10.1007/s42235-021-00088-7.

[18] J. Dirks, M. Li, A. Kabla, W. Federle, In vivo dynamics of the internal fibrous structure in smooth adhesive pads of insects, Acta Biomater. 8 (7) (2012) 2730–2736, https://doi.org/10.1016/j.actbio.2012.04.008.

[19] D. Labonte, M.Y. Struecker, A.V. Jeffery, W. Federle, Shear-sensitive adhesion enables size-independent adhesive performance in stick insects, Phil. Trans. R. Soc. B 286 (2019), 20191327, https://doi.org/10.1098/rspb.2019.1327.

[20] L. Xue, B. Sanz, A. Luo, K.T. Turner, X. Wang, D. Tan, R. Zhang, H. Du, M. Steinhart, C. Mijangos, M. Guttmann, M. Kappl, A. Del Campo, Hybrid surface patterns mimicking the design of the adhesive toe pad of tree frog, ACS Nano 11 (10) (2017) 9711–9719, https://doi.org/10.1021/acsnano.7b04994.

[21] D.M. Drotlef, E. Appel, H. Peisker, K. Dening, A. Del Campo, S.N. Gorb, W.J.P. Barnes, Morphological studies of the toe pads of the rock frog,Staurois parvus (family: ranidae) and their relevance to the development of new biomimetically inspired reversible adhesives, Interface Focus 5 (1) (2015), 20140036, https://doi.org/10.1098/rsfs.2014.0036.

[22] V. Mizuhira, The digital pads of rhacophorid tree-frogs, J. Electron. Microsc. 53 (1) (2004) 63–78, https://doi.org/10.1093/jmicro/53.1.63.

[23] W. Federle, E.L. Brainerd, T.A. McMahon, B. Holldobler, Biomechanics of the movable pretarsal adhesive organ in ants and bees, Proc. Natl. Acad. Sci. U. S. A 98 (11) (2001) 6215–6220, https://doi.org/10.1073/pnas.111139298.

[24] M. Holtje, R. Hustert, Rapid mechano-sensory pathways code leg impact and elicit very rapid reflexes in insects, J. Exp. Biol. 206 (16) (2003) 2715–2724, https://doi.org/10.1242/jeb.00492.

[25] J. Michels, S.N. Gorb, Detailed three-dimensional visualization of resilin in the exoskeleton of arthropods using confocal laser scanning microscopy, J. Microsc. 245 (1) (2012) 1–16, https://doi.org/10.1111/j.1365-2818.2011.03523.x.

[26] M. Bennemann, S. Backhaus, I. Scholz, D. Park, J. Mayer, W. Baumgartner, Determination of the Young's modulus of the epicuticle of the smooth adhesive organs of Carausius morosus by tensile testing, J. Exp. Biol. (2014), https://doi.org/10.1242/jeb.105114.

[27] K. Kendall, Thin-film peeling-the elastic term, J. Phys. D Appl. Phys. 8 (13) (1975) 1449–1452, https://doi.org/10.1088/0022-3727/8/13/005.

[28] J. Liu, R. Xia, A unified analysis of a micro-beam, droplet and CNT ring adhered on a substrate: calculation of variation with movable boundaries, Acta Mech. Sin. 29 (1) (2013) 62–72, https://doi.org/10.1007/s10409-012-0202-8.

[29] R.A. Sauer, The peeling behavior of thin films with finite bending stiffness and the implications on gecko adhesion, J. Adhes. 87 (7–8) (2011) 624–643, https://doi.org/10.1080/00218464.2011.596084.

[30] L. Frantsevich, S. Gorb, Arcus as a tensegrity structure in the arolium of wasps (Hymenoptera: vespidae), Zoology 105 (3) (2002) 225–237, https://doi.org/10.1078/0944-2006-00067.

[31] L. Frantsevich, S. Gorb, Structure and mechanics of the tarsal chain in the hornet, Vespa crabro (Hymenoptera: vespidae): implications on the attachment mechanism, Arthropod Struct. Dev. 33 (1) (2004) 77–89, https://doi.org/10.1016/j.asd.2003.10.003.

[32] M. Burrows, S.R. Shaw, G.P. Sutton, Resilin and chitinous cuticle form a composite structure for energy storage in jumping by froghopper insects, BMC Biol. 6 (1) (2008), https://doi.org/10.1186/1741-7007-6-41, 41-41.

[33] G. Qin, X. Hu, P. Cebe, D.L. Kaplan, Mechanism of resilin elasticity, Nat. Commun. 3 (1) (2012), https://doi.org/10.1038/ncomms2004.

[34] C. Schmitt, O. Betz, Morphology and ultrastructure of the tarsal adhesive organs of the Madagascar hissing cockroach Gromphadorhina portentosa, Cell Tissue Res. 370 (2) (2017) 243–265, https://doi.org/10.1007/s00441-017-2661-5.

[35] D. Shin, W.T. Choi, H. Lin, Z. Qu, V. Breedveld, J.C. Meredith, Humidity-tolerant rate-dependent capillary viscous adhesion of bee-collected pollen fluids, Nat. Commun. 10 (1) (2019), https://doi.org/10.1038/s41467-019-09372-x.

[36] L. Zhang, H. Chen, Y. Guo, Y. Wang, Y. Jiang, D. Zhang, L. Ma, J. Luo, L. Jiang, Micro-nano hierarchical structure enhanced strong wet friction surface inspired by tree frogs, Adv. Sci. 7 (20) (2020), 2001125, https://doi.org/10.1002/advs.202001125.

[37] A.C. Neville, The Biology of the Arthropod Cuticle, Springer Berlin Heidelberg, 1975.

[38] S.B. Segletes, W.P. Walters, A note on the application of the extended Bernoulli equation, Int. J. Impact Eng. 27 (5) (2002) 561–576, https://doi.org/10.1016/S0734-743X(01)00153-1.

[39] L. Elkarous, A. Nasri, R. Nasri, Numerical modeling and analysis of the pressure pulses generator for the dynamic calibration of high-pressure transducers, Appl. Acoust. 147 (2019) 56–63, https://doi.org/10.1016/j.apacoust.2018.04.015.